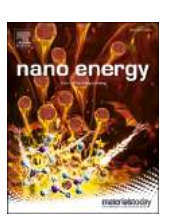
ELSEVIER

Contents lists available at ScienceDirect

Nano Energy

journal homepage: www.elsevier.com/locate/nanoen





Effect of pore structure on the piezoelectric properties of barium titanate-polyvinylidene fluoride composite films

Tim Kowalchik ^a, Fariha Khan ^b, Katrina Le ^a, Paige Leland ^a, Shad Roundy ^a, Roseanne Warren ^{a,*}

- ^a Department of Mechanical Engineering, University of Utah, 1495 E 100 S, 1550 MEK, Salt Lake City, UT 84112, USA
- b Department of Electrical and Computer Engineering, University of Utah, 50 S. Central Campus Drive, MEB Room 2110, Salt Lake City, UT 84112, USA

ARTICLE INFO

Keywords:
Phase behavior
Piezoelectricity
Polymer composites
Thin films
Mechanical response

ABSTRACT

Piezoelectric voltage generation in porous barium titanate-poly(vinylidene fluoride) (BT-PVDF) particle-matrix composite films is investigated as a function of PVDF pore structure and porosity. BT-PVDF composite films fabricated *via* coagulation bath method attain distinct pore structures depending on the ethanol content of the bath. With increasing bath ethanol content, film morphology shifts from higher porosity finger-like cavities to lower porosity mesh-like structures. Finger-like films have a lower Young's modulus than mesh-like films (224 MPa *vs.* 368 MPa), but produce higher piezoelectric output voltage when compressed compared to mesh-like films (400 mV *vs.* 57 mV under 3 N compression). The difference in piezoelectric response is attributed to differences in stress transfer between polymer matrix and ceramic particles. Finite element simulations reveal that finger-like structures produce well-ordered compressive stress while mesh-like structures produce poor stress alignment. The results indicate that improved stress transfer between polymer matrix and ceramic particles can be achieved with well-aligned pore structures, leading to higher piezoelectric output.

1. Introduction

Poly(vinylidene fluoride) (PVDF) is a piezoelectric polymer with excellent mechanical flexibility, chemical inertness, and ease of fabrication as a piezo-active thin film. Compared to crystalline or ceramic piezoelectrics, however, PVDF has lower stiffness and piezoelectric strain coefficients (d_{xx}) , leading to lower piezo-active response. One method to increase PVDF piezoelectric performance is to create composite films with ceramic filler particles, such as barium titanate-PVDF (BT-PVDF) [1]. Among piezoelectric ceramics available for PVDF composites, BT is desirable for its ease of fabrication, demonstrated ability to increase β-phase content in PVDF, good piezoelectric properties, and low cost [2,3]. Although lead-based fillers such as lead zirconate titanate (PZT) have superior piezoelectric properties, the presence of toxic lead in these materials limits use cases heavily [4]. BT-PVDF composites demonstrate improved piezoelectric response due to the increased piezo-activity of the filler particle, while retaining the mechanical flexibility of the polymer matrix [5]. To-date, composite piezo-active films have found use in applications including motion and pressure sensors [6,7], prospective medical implants like pacemakers [8], and flexible energy harvesters [9,10]. In addition to good piezoelectric response, many applications of piezo-active films require porous piezoelectric materials, *e.g.* tissue repair scaffolding [11], "self-charging power cells" [12], and liquid or gas filtration devices [13]. Despite the requirement for high porosity and the importance of good piezoelectric response in such applications, to date there have been no investigations of process-structure-property relationships for porous BT-PVDF composites, including the impact of PVDF pore morphology on stress transfer through the matrix.

Previous studies have elucidated many important structure-property relationships of porous piezoelectric materials, including relationships between pore structure and piezoelectric activity. Porous structures are generally more flexible than the bulk material. As a result, larger strains and voltage outputs can be expected for similar forces with small-to-moderate levels of porosity [14]. The addition of nanopores in BT was found to improve d_{33} output by 35% when compared to dense material [15]. Structured nanopores introduced into PVDF were able to boost piezoelectricity by 6x over bulk material [16]. With increasing pore size and porosity, however, the material may begin to lose piezoelectric performance compared to the bulk [17–19]. During modification of PZT density for acoustic use, introducing 45% porosity in the PZT reduced piezoelectric d_{33} by 40% compared to 5% porous PZT [20]. When

E-mail address: roseanne.warren@utah.edu (R. Warren).

^{*} Corresponding author.

annealing sputtered zinc oxide thin films at different temperatures to control porosity, piezoelectric voltage response increased by 2.5x for 45 nm pores compared to bulk zinc oxide, before decreasing to 0.5x as pore size increased to 90 nm [21]. Pore structure and ordering also influence piezoelectric response, with smaller, highly ordered pores often increasing piezo-activity compared to larger, disordered pores. When structured by freeze-templating, the most highly ordered middle region of porous PZT had higher piezoelectric response than the disordered top and bottom regions [22]. Porosity may also affect piezoelectric materials by lowering capacitance, inducing fatigue, and increasing risk of dielectric breakdown [23,24]. The presence of these complex factors necessitates experimental study of process-structure-property relationships in porous piezoelectric materials.

Despite the challenges porosity may introduce into piezoelectric materials, many applications require piezoelectric films to also function such as electrochemical separators or filtration devices. Porous piezoelectric membranes can lower filtration pressure and membrane fouling, control biological substances, or influence electro-chemical processes [25–28]. For applications where a piezoelectric film is required to be

porous, it is crucial that the piezoelectric activity remain strong after porosity is introduced.

Phase inversion is a well-studied method to create controlled pores in polymer thin films [29]. In phase inversion, the casting solvent is replaced with a secondary non-solvent or non-solvent mixture in a coagulation bath. The resulting demixing process produces a porous film, with the specific structure depending on the choice of solvent, non-solvent, and polymer [30]. Phase inversion is a facile method of achieving porosities greater than 60% in thin polymer films. Previous studies of PVDF coagulation baths have identified two pore structures that form in the polymer matrix: finger-like channels and interconnected mesh. Adding ethanol to the non-solvent deionized (DI) water bath directs pore structure depending on the ratio of ethanol-to-water. Previous experiments have established that increasing ethanol content produces more interconnected mesh vs. finger-like structures in PVDF [28-33]. The effect results from the speed with which phase inversion occurs in pure DI water vs. ethanol-water mixture, with the slower ethanol-solvent interaction allowing mesh structures to form in the PVDF. To date, phase inversion has not been applied to ceramic-polymer composite

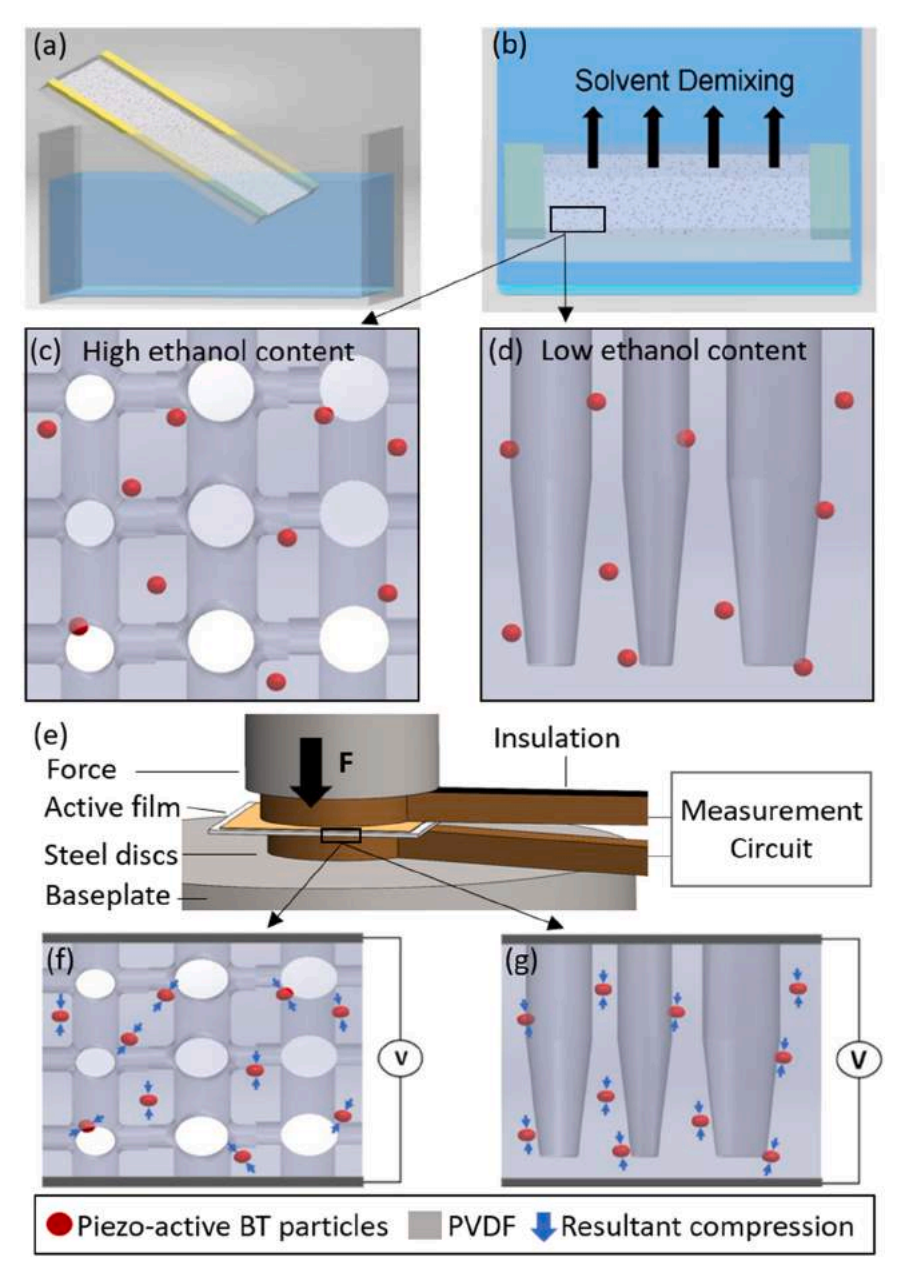


Fig. 1. a, b) Fabrication of porous piezo-active BT-PVDF composite films by phase inversion. c) Mesh-like pore structures result from high ethanol content in the coagulation bath. d) Finger-like structures form with low ethanol content. e) During piezoelectric testing, force is applied to the top surface of the films resulting in compressive force on the BT particles. BT-PVDF interaction is expected to vary with mesh (f) vs. finger-like (g) morphologies. Note: Geometry shown is idealized for the extremes of the two structures; real geometry is much less ordered.

T. Kowalchik et al. Nano Energy 109 (2023) 108276

piezoelectric thin films, and questions remain as to the effect of this method on the porous structure and resulting piezo-activity of the composite. For BT-PVDF composites, interconnected mesh and finger-like pore structures are expected to have distinctly different mechanical properties that will impact piezoelectric voltage generation from the ceramic filler particles.

This work investigates, for the first time, the effect of pore structure on the piezoelectric activity of BT-PVDF composite films produced by phase inversion. By varying the ethanol-water ratio of the phase inversion process, BT-PVDF composite films with different pore structures are created (Fig. 1 a-d). The effect of pore structure on the mechanical properties and the piezoelectric voltage response of the composite films is examined when the films are subject to compressive loading (Fig. 1eg). The results are correlated with pore structure and porosity with the aid of finite element simulations. A transition from finger-like structures to interconnected mesh is observed in the BT-PVDF composites as ethanol concentration increases, resulting in increasing Young's modulus and lower voltage output under compressive loading. Despite lower Young's modulus, finger-like structures are found to be most effective for achieving high piezoelectric response and good porosity for the flexible, composite structures. This study highlights the fact that a 7X increase in piezoelectric voltage output can be achieved in porous piezoelectric composite films by paying close attention to pore structure without changing any of the constituent materials. It is anticipated that the results presented here can guide future designs of highly porous ceramic-polymer piezoelectric materials synthesized by phase inversion, including ceramic and polymer materials extending beyond BT and PVDF.

2. Methods

2.1. BT-PVDF porous film fabrication

BT particles were purchased from Stanford Advanced Materials (BaTiO₃, tetragonal structure, typical size from scanning electron microscopy (SEM) images: 150 nm). All other materials were purchased from Millipore-Sigma and used as received. PVDF powder (average MW~534,000 g/mol) was dissolved in N, N-dimethylformamide (DMF) at 12% w/w in a 45 $^{\circ}$ C water bath. Large agglomerations of BT particles were lightly broken down using a spatula, and a suspension of BT particles was created in DMF such that the PVDF/DMF ratio was 15% w/w (7% v/v) once mixed. BT was suspended in 20% of the total DMF. BT mass loading was 20% w/w vs. PVDF (2.5-3.1% v/v depending on film porosity). BT-DMF and PVDF-DMF suspensions were continuously mixed for 1 h. The homogeneous BT dispersion was added to the PVDF-DMF solution at room temperature, mixed for 5 min to combine, and sonicated for 1 h to ensure homogeneity. BT-PVDF films were made by drop-casting the prepared slurry onto a glass plate using a doctor blade and Kapton tape to obtain uniform thicknesses. The coated glass plates were immediately immersed in the prepared coagulation baths for 20 min at room temperature. Coagulation baths were prepared with DI water: ethanol w/w ratios of 100:0 ("DI"), 85:15 ("DI15E"), 70:30 ("DI30E") and 55:45 ("DI45E"). The films were dried at 60 $^{\circ}\text{C}$ in an oven to evaporate the DMF, then annealed for 5 h at 90 °C in the oven directly after drying. An electric field of 15 MV/m was applied for 60 min to pole the films. Films were immersed in a silicone oil bath during poling. The temperature was maintained at 120 °C for the first 30 min of poling, followed by a 30 min cooling period under the same electric field. Two stainless steel plates (2 mm thickness, contact area 75 mm \times 50 mm) were used as electrodes for poling. A commercial, non-porous, piezoelectric PVDF film was purchased from TE Connectivity (52 µm thickness) and tested under the same conditions as the BT-PVDF films.

2.2. Characterization

BT-PVDF film morphology was characterized by SEM imaging using

an FEI Quanta 600 F. To obtain clean cross-sections, the films were immersed in liquid nitrogen prior to breaking. Cross-sectional SEM images were taken close to the center of each 60 mm \times 30 mm film sample. Pore size values reported from SEM images were obtained by averaging twenty pore size measurements taken from two different samples for each ethanol bath concentration (ten measurements per film sample). BT particle distribution was qualitatively examined through energy dispersive X-ray spectroscopy (EDS). Fourier transform infrared spectroscopy (FTIR) measurements obtained using a Varian 3100 Excalibur FTIR were used to measure BT and β phase content of BT-PVDF films.

BT-PVDF film porosity was measured by immersing the films in 1-butanol for 1 h, with the mass of the films measured before and after immersion [32]. Porosity (ϵ) was calculated using Eq. 1:

$$\varepsilon = \frac{\frac{m_b}{\rho_b}}{\frac{m_p}{\rho_p} + \frac{m_b}{\rho_b}} \tag{1}$$

where ρ_p, ρ_b are the densities of PVDF and 1-butanol, respectively, and m_p, m_b are the mass of the dry film and film after soaking, respectively. Young's moduli (*E*) of BT-PVDF films were measured with an Instron 5969 using a 1 kN load cell. Dog bone-shaped film samples (9 mm \times 20 mm) were subjected to < 2% strain to be in the elastic region of the stress-strain curve. Young's moduli of the films in tension were extracted from stress-strain measurements following Eq. 2:

$$E = -\frac{\sigma}{c} \tag{2}$$

where σ is applied stress, and ε is strain calculated from total elongation and initial length. BT-PVDF films were electroded for piezoelectric measurement using a sputtered gold layer on both sides. Custom 3D-printed clamps were used to secure BT-PVDF films in the Instron. The voltage response of the films under tensile stress was measured by applying 1–2% strain along the length of the film. For compressive stress testing, electroded samples were placed between two metal discs of 176 mm², insulated from the Instron surfaces. Force was applied to the metal discs in the Instron resulting in compressive stress through the film thickness. The films were stressed at 1, 3, 5, 10, and 20 N forces over 10 cycles each to test open circuit voltage response and deformation. Before each test, contact was made between the metal discs and the film through light compression until no gaps were visible. Voltage response was measured for the non-porous film under the same conditions.

2.3. Simulation

Finite element simulations were used to examine the stress and strain responses of finger- and mesh-like porous PVDF structures under compressive loading. Porous geometries approximating finger- and mesh-like structures were modeled using SolidWorks and imported into COMSOL Multiphysics® finite element software. Finger-like pore structures were approximated as tapered elliptical cylinders with 15 \pm 5 μm average upper diameter, 7.5 \pm 1 μm average lower diameter, and uniform 42 µm height along the film thickness. Mesh-like pore structures were approximated as an array of holes with 22 \pm 10 mm average diameter interconnected by cylinders with 8.5 \pm 3 mm average diameter, randomly placed within a grid cell. All simulated films were $2500 \,\mu\text{m}^2$ by $50 \,\mu\text{m}$ thick, with total film porosity matching average experimental measurements of finger- and mesh-like porous BT-PVDF films. The following properties of PVDF were used in the simulations: 1780 kg/m³ density, 2.45 GPa Young's modulus, 0.34 Poisson's ratio. Sub-micron pores and BT particles were neglected in the simulations. A modified fine meshing was used in all simulations. The x, y, and z axes were taken as the 1, 2, and 3 directions of principal stress, respectively. A 20.8 kPa compressive stress was uniformly applied to each simulated geometry to match the stress applied during 3 N Instron tests. Sidewall

boundaries were allowed to freely deform while the bottom surface was fixed. Finite element simulation results were extracted from the center of the simulated films, where sidewall deformation effects were negligible.

3. Results and discussion

Fig. 2 presents cross-sectional SEM images of BT-PVDF films fabricated under four coagulation bath water: ethanol weight ratios: DI (Fig. 2a), DI15E (Fig. 2b), DI30E (Fig. 2c); and DI45E (Fig. 2d). SEM images in Fig. 2 are aligned with film orientation during drop-casting (i. e. the "top" surface in the images was at the solution-air interface during fabrication, and the "bottom" surface in the images was positioned along the glass slide). All films are $50\,\mu m$ thick. The films show a trend of finger-like to mesh-like structure conversion as bath ethanol content rises. DI films (Fig. 2a) are characterized by finger-like structures running vertically from the top to bottom surface of the film. The average width of the finger-like structures is 8.50 \pm 1.10 $\mu m;$ smaller circular pores within those structures have $0.82 \pm 0.13\,\mu m$ average diameter. DI15E films (Fig. 2b) have finger-like structures confined to the top half of the films, with mesh-like structures present in the bottom half. The average width of the finger-like structures is less than that of DI films (3.84 \pm 0.95 μ m). Smaller circular pores in both upper and lower regions of the DI15E films have also decreased in size, with an average diameter of 0.68 \pm 0.15 $\mu m.$ Above 30% ethanol content (DI30E and DI45E films), finger-like structures are not found anywhere along the cross-sectional images, and the film structure becomes entirely meshlike (Fig. 2c, d). The average pore size of the mesh-like films is 0.55 \pm 0.28 µm and 0.58 \pm 0.31 µm for DI30E and DI45E films, respectively.

Pore formation in coagulation baths, including pore structure and size, depends on the solvent-nonsolvent exchange rate in the phase inversion processes. The exchange rate of PVDF is highest in pure DI water. With the addition of the ethanol, solvent-non-solvent mixing is

reduced and the exchange rate of PVDF decreases [31]. This results in the different morphologies observed in the films. Increasing PVDF exchange rate produces larger and more continuous pores (i.e. finger-like structures in Fig. 2a, b). In Fig. 2b, finger-like structures preferentially form at the polymer-non-solvent interface, where solvent/non-solvent mixing occurs more rapidly than at the polymer-glass interface. To ensure repeatability of the observed pore structures, three independently prepared films were imaged for each of the coagulation bath conditions. Similar trends in pore structure and size were observed in all three batches of films.

The results presented in Fig. 2 for BT-PVDF composite films match previous studies of coagulation bath pore formation with pure PVDF films [30-33], indicating that the introduction of 20 wt% BT particles does not visibly affect the phase inversion process of PVDF. At 20 wt% BT, no agglomeration of BT particles is observed in the porous films and BT appears well-spread. EDS measurements of DI films reinforce these conclusions, showing evenly distributed BT particles throughout the film cross-section (Supporting Information Fig. S1). The liquid-liquid demixing mechanism overcomes the localized impact of BT particles on the surrounding matrix, making coagulation baths a good approach for guiding porous composite film structure. FTIR results indicate similar BT loading within each film type (Supporting Information Fig. S2). A second set of FTIR measurements comparing DI, DI45E, and nonporous BT-PVDF films shows similar PVDF phases, indicating comparable quantities of electroactivity for each film type (Supporting Information Fig. S3).

Table 1 provides average porosity and Young's modulus measurements for BT-PVDF films prepared under varying coagulation bath conditions. Average values are obtained using three films prepared independently. The results are plotted in Fig. 3 to show relationships between: i) coagulation bath ethanol content and film porosity, and ii) Young's modulus and film porosity. Young's modulus was calculated

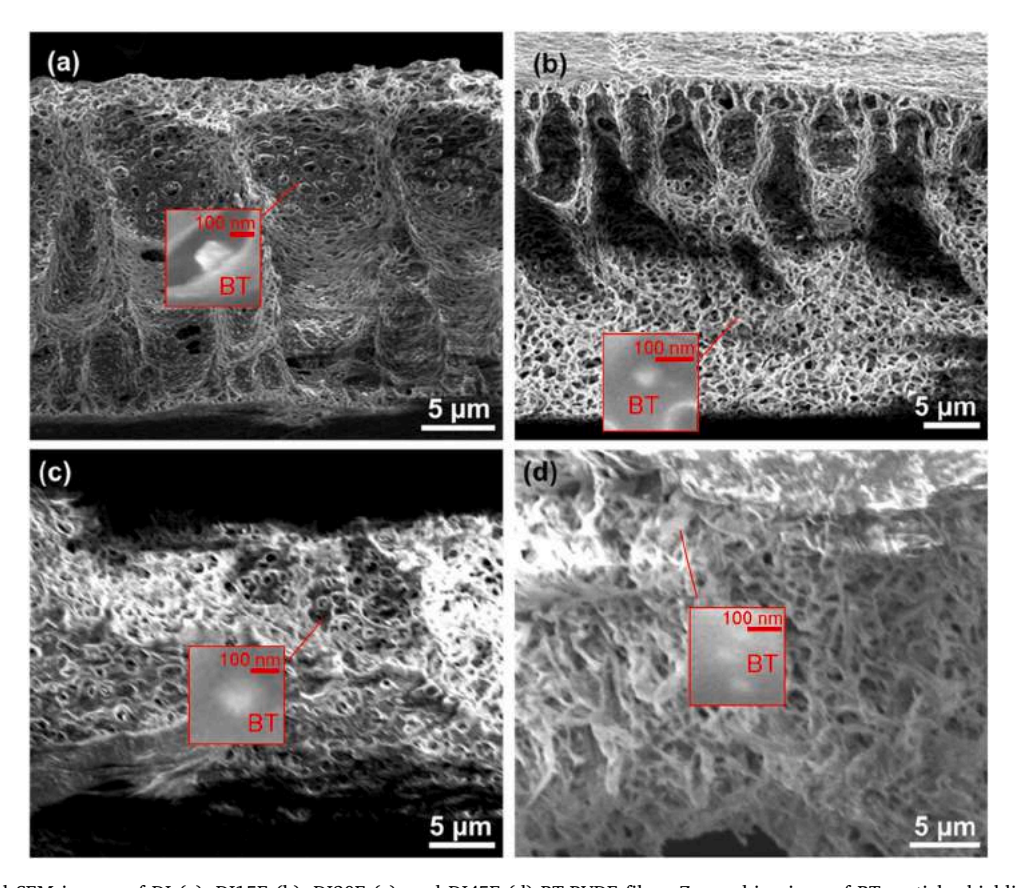


Fig. 2. Cross-sectional SEM images of DI (a), DI15E (b), DI30E (c), and DI45E (d) BT-PVDF films. Zoomed-in views of BT particles highlighted in red for each cross-section.

Table 1Average film porosity and Young's modulus of BT-PVDF films prepared under varying coagulation bath conditions compared with commercial, non-porous PVDF.

Coagulation bath conditions	Porosity (%)	E (MPa)
DI	64.91 ± 0.41	224 ± 12
DI15E	63.30 ± 0.87	251 ± 3
DI30E	60.33 ± 1.15	310 ± 10
DI45E	58.20 ± 1.45	368 ± 2
Commercial PVDF	2.5	2000

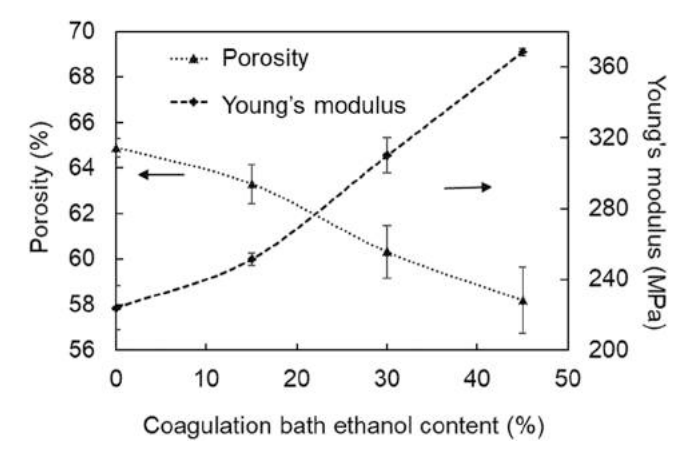


Fig. 3. Effect of coagulation bath ethanol content on the porosity and Young's modulus of BT-PVDF films. Increasing ethanol content results in decreasing porosity and increasing Young's modulus.

from tensile stress-strain curves (Supporting Information Fig. S4). A negative correlation is observed between coagulation bath ethanol content and film porosity. This is likely due to the conversion of larger finger-like pore structures to smaller mesh-like pores with increasing ethanol content (Fig. 2). However, despite the decrease in porosity, even the DI45E film has high porosity near 60%, with all other films remaining above 60% porosity. With decreasing porosity and pore size, we observe an increase in Young's modulus of the films. This trend matches expectations for porous films, as more material necessarily provides more resistance to applied force. The relationship between porosity and Young's modulus is directly inversely proportional. Within the range of porosities tested, relatively small changes in film porosity coincide with large changes in Young's modulus; for example, a 7% decrease in the absolute value of porosity from DI to DI45E samples coincides with a 64% change in Young's modulus from 224 MPa to 368 MPa. The Young's modulus of the commercial PVDF film (2.5%

porosity) is 2 GPa; as expected, the porous films are significantly more compliant than the non-porous film.

The piezoelectric performance of the BT-PVDF films was tested under compressive and tensile loading conditions. Under compressive loading, the porous structure of the films permanently deformed when the applied compressive force was 10 N or higher. At greater than 10 N loading, the piezoelectric voltage decreased with every cycle and the films became effectively non-responsive after $\sim\!30$ cycles. SEM inspection after compression at ≥ 10 N loading confirmed the permanent deformation of porous structures in all films. All subsequent compressive testing was performed at lower forces to ensure sustained voltage output with repeated cycling. Under tensile loading, all four BT-PVDF film morphologies produced low peak-to-peak voltage (Vpp) output (10–20 mV under tensile strain of 1–2%). We believe this is due to poor stress transfer from the PVDF matrix to the BT particles in the longitudinal direction.

Fig. 4a plots the open circuit piezoelectric voltage response of a DI film under 3 N of cyclic compressive force. The film produced a stable V_{pp} response of 400 mV over the ten cycles measured. Similar voltage profile shapes were observed for all other BT-PVDF films under the same loading conditions. Under higher compressive loading conditions (e.g. \geq 5 N), V_{pp} decreases over the first several loading cycles, likely due to irreversible changes to film porous structure (Supporting Information Fig. S5). V_{pp} for DI and DI30E films was measured and recorded over a five-day period to observe the stability of the response with time. No decrease in V_{pp} response was observed (Supporting Information Table S1).

Fig. 4b compares the average piezoelectric V_{pp} response of the BT-PVDF films over ten loading-unloading cycles as a function of porosity under 3 N compressive loading. Two unexpected results are observed. First, piezoelectric voltage response is highest for DI and DI15E samples, despite their lower Young's modulus. We would expect higher Young's modulus films to transfer stress more readily to BT particles, resulting in higher piezoelectric output in the mesh-like DI30E and DI45E samples. Of particular note is the sharp decrease in piezoelectric voltage response observed when the finger-like structures disappear between the DI/ DI15E and DI30E/DI45E pairings (Fig. 4b). Second, the magnitude of the observed increase in V_{pp} with increasing porosity is larger than might be expected given the relatively modest changes in porosity and Young's modulus. A 6.7% absolute decrease in porosity from DI to DI45E coincides with an increase in Young's modulus from 224 MPa to 368 MPa (~1.6x greater). However the DI film produces 7x V_{pp} output compared to the DI45E film, with corresponding piezoelectric charge coefficients $d_{33}=66$ pC/N (DI) and $d_{33}=9.4$ pC/N (DI45E). DI and DI15E films have piezoelectric charge coefficients greater than commercial, non-porous PVDF (d₃₃ =33 pC/N); DI30E and DI45E have piezoelectric charge coefficients less than the commercial, non-porous film (Table 2). Compared to other piezoelectric materials, the DI film

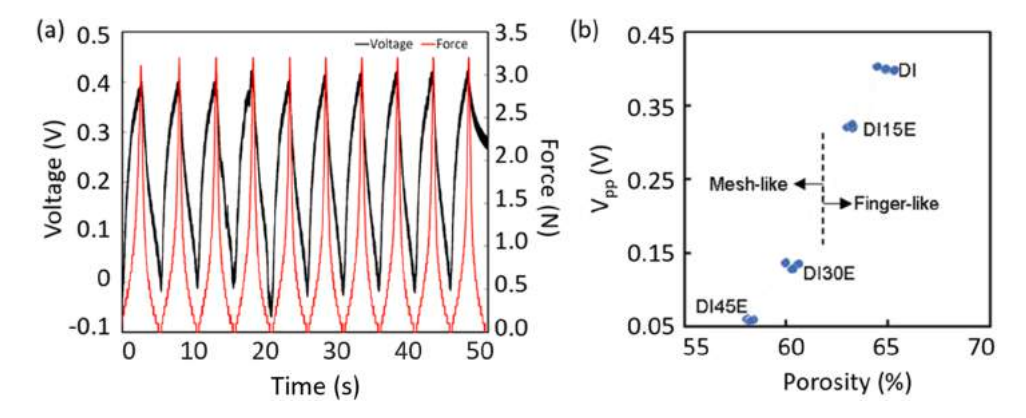


Fig. 4. a) Piezoelectric voltage response of the DI film under compressive loading. b) Voltage response (V_{pp}) vs. BT-PVDF film porosity under 3 N compressive loading. Data points are plotted for each sample measured.

Table 2 Average piezoelectric d_{33} coefficients of commercial, non-porous PVDF and porous BT-PVDF composite films.

Material	d ₃₃ (pC/N)
Commercial PVDF (datasheet value)	33
Unpoled BT-PVDF	< 1
DI	66.0
DI15E	55.3
DI30E	20.6
DI45E	9.4

has a comparable d_{33} to other polymer-ceramic composites reported in literature (Supporting Information Table S2). As a secondary check on mechanical properties and V_{pp} , the compliance of each film was plotted $vs.\ V_{pp}$ (Supporting Information Fig. S6). As with the porosity relationship in Fig. 4b, there is a noted discontinuity in V_{pp} vs. compliance observed at the transition point from mesh-like to finger-like pore structures. It is hypothesized that these observations can be attributed to differences in the interaction between ceramic BT particles and the PVDF polymer matrix that arise with different film morphologies. Unpoled films for each coagulation bath have $d_{33} < 1$ pC/N, and produce negligible piezoelectric voltage response.

Electrostatic poling of PVDF films is typically performed at 50–120 MV/m [34,35], while sub-micron BT particles may be poled

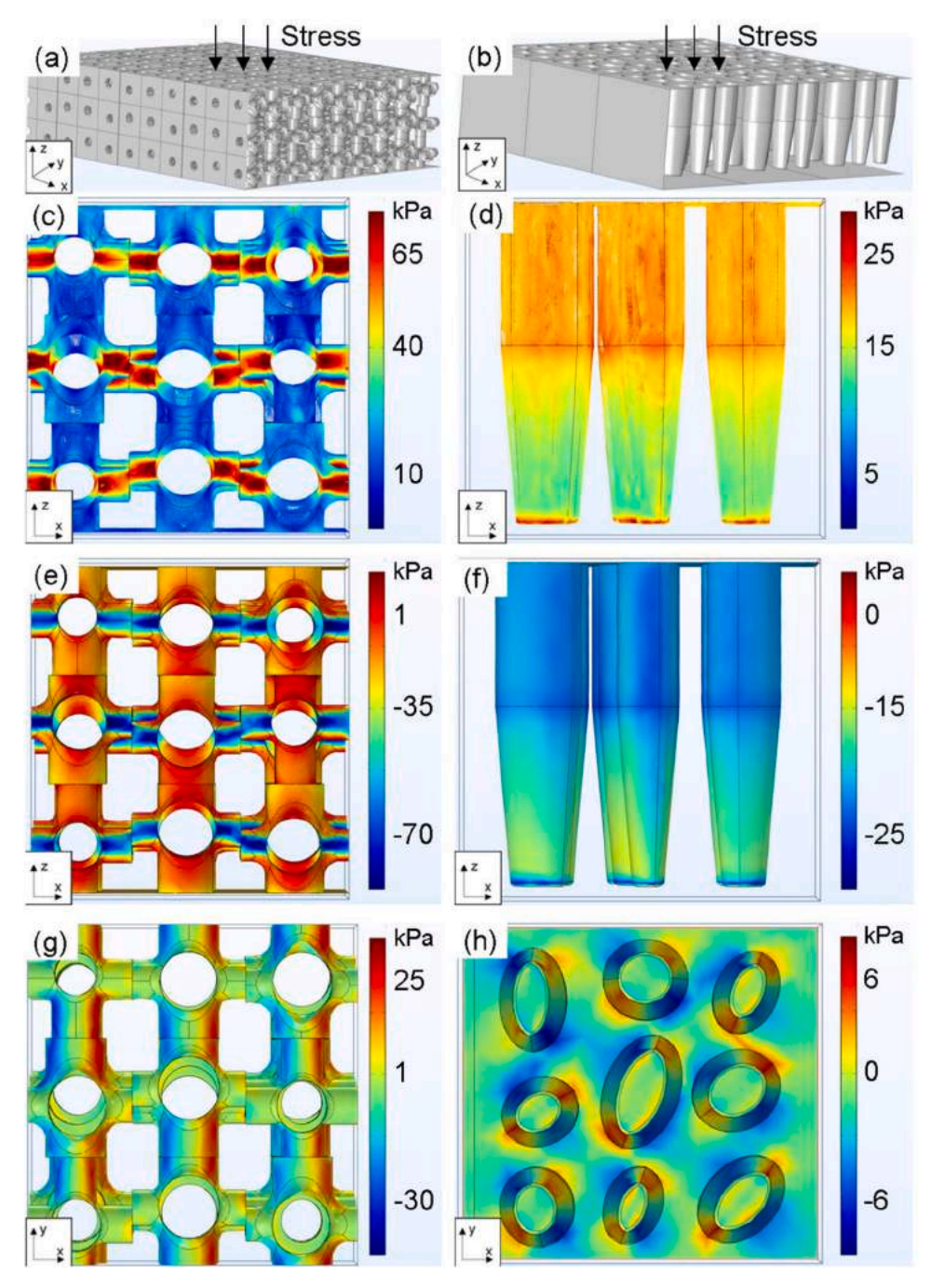


Fig. 5. Simulation results for mesh-like (left) and finger-like (right) PVDF structures under 20.8 kPa compressive stress. a, b) CAD model of the simulated film structures. Compressive stress is applied to the top surface. c, d) Surface contour plots of von Mises stress in the x-z plane. e, f) Compressive stress (principal 3 direction) surface plot in the x-z plane. g, h) 2–3 shearing stress top view surface plot in the x-y plane.

near 10 MV/m [36,37]. Introducing porosity into BT-PVDF films through coagulation baths makes electrostatic poling substantially more difficult, with dielectric breakdown commonly observed even at relatively low applied fields. For porous BT-PVDF films, dielectric breakdown was observed at poling fields > 16 MV/m. Under the poling conditions applied in this study (15 MV/m), the PVDF matrix is assumed to be weakly poled, with the majority of the piezoelectric response arising from the BT particles. This was confirmed by measuring the piezoelectric response of: (i) unpoled BT-PVDF films, and (ii) pure PVDF films poled at 15 MV/m. For every ethanol concentration, all unpoled films showed negligible voltage response ($\rm V_{pp} < 1~mV$).

Given that most of the piezoelectric voltage response of the porous composite films arises from the BT particles, the ability to effectively transfer stress from the polymer matrix to the ceramic particles is of great importance for achieving high piezoelectric response with the porous, composite films. The higher piezoelectric voltages measured for finger-like pore structures vs. mesh-like pores (Fig. 4b) suggest that more effective stress transfer to the BT particles occurs with the finger-like structure vs. interconnected mesh. We propose two possible mechanisms by which the polymer pore structure affects stress transfer to the ceramic particles: 1) variations in stress states around pores due to differences in stress between the two structures, and 2) changing BT particle orientation during deformation. These mechanisms are explored through finite element simulations of mesh- and finger-like pore structures under compressive loading.

Fig. 5a, b illustrates the simulation geometry used to compare differences in mechanical loading response between mesh- and finger-like pore structures. Sub-micron pores present throughout mesh- and finger-like structures are neglected in the models. Due to similarities in sub-

micron pore size and distribution in mesh- and finger-like structures, it is unlikely that these pores give rise to the differences in voltage output observed experimentally. BT particles are also neglected in the simulations. Differences in stress profiles throughout the matrix are used to infer the piezoelectric output of BT particles at those locations.

Fig. 5c, d provide contour plots of von Mises stresses in mesh- and finger-like pores, respectively. The mesh-like structure presents significant von Mises stresses along the horizontal connections between cavities, indicating a high degree of distortion in these regions (Fig. 5c). The finger-like structure shows a consistently decreasing von Mises stress level through the thickness of the film, increasing only at the very bottom of the cavities (Fig. 5d). Fig. 5e, f plot principal stress in the z direction (i.e. compression through the thickness). The results indicate that compressive stress is higher for the finger-like structure (-11.13)kPa) than the mesh-like structure (-7.16 kPa). Shear stress plots (Fig. 5g, h) indicate that the mesh-like structure has large alternating shear along the horizontal pore connections, while the finger-like structure shows little shearing. Overall, stress states within the fingerlike structure appear more uniformly compressive, and will stress BT particles primarily in alignment with their poling direction. Within the mesh-like structure, horizontal connections between cavities allow large stresses to form in a multitude of directions. BT particles will be stressed in compression, however there will be larger variations in total stress directions reducing the corresponding piezoelectric voltage.

The above observations are further illustrated by comparing principal stress directions along pore cross-sections (Fig. 6). Fig. 6a, b show the simulated geometries, including x-y and x-z planes. Subsections for calculation of principal stresses were taken from a central portion of the matrix, halfway through the thickness. Fig. 6c, d illustrate principal

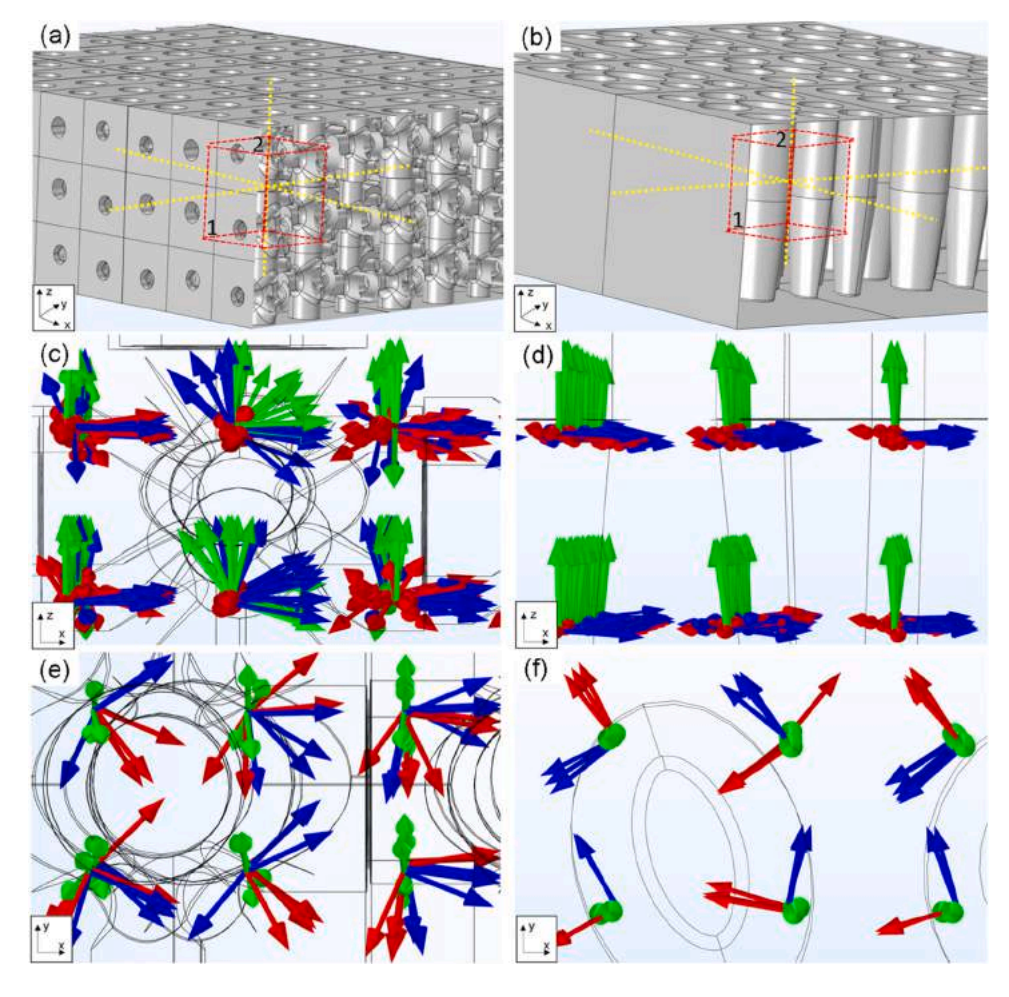


Fig. 6. Simulation results of mesh- (left) and finger-like (right) PVDF structures under 20.8 kPa compressive stress. a, b) Partial cross-section of the simulated structure, with sampling region highlighted. c, d) Principal stress variation along y, as viewed into the x-z plane. Red arrows – principal 1, blue arrows – principal 2, green arrows– principal 3. e, f) Principal stress variation along z, as viewed into the x-y plane. Principal stress directions are poorly aligned in the mesh-like structure compared to the finger-like structure.

stress vectors viewed into a cross-section of the mesh- and finger-like structures, respectively (i.e. view into the x-z plane). Principal stress arrows show normal stress directions for each plane where shear stress is zero. While both finger- and mesh-like structures show some stress concentrations directed towards open cavities, important differences can be seen in the consistency of principal stress vector alignment with finger- vs. mesh-like pores. Finger-like pore structures produce good stress alignment down the entire length of the pores until the bottom of the fingers is reached. It is hypothesized that this will induce a more directionally-consistent stress on the BT particles throughout the film that is aligned with the particle poling direction, reinforcing the compressive results seen in Fig. 5e, f. Principal stresses experienced by the mesh-like structure are less well-aligned, with principal stress vectors in Fig. 6c: i) pointing in multiple directions at a given depth, and ii) shifting in direction throughout the film cross-section.

A view through the film thickness (i.e. into the x-y plane) shows the shifting alignment of principals 1 and 2 in the mesh structure (Fig. 6e). Arrows are fanned across arcs from 90° to 180° through the thickness, indicating large shifts in stress directionality with no consistent pattern. The finger-like structure shows much tighter grouping of principal stress arrows, with each principal stress largely in the same orientation among pores and through the film thickness (Fig. 6f). When deformed, it is likely that the mesh-like structure strains in non-uniform directions in contrast to the more uniform deformation of the finger-like structure, giving rise to the large differences in shear and von Mises stresses seen in Fig. 5.

These simulation results indicate two primary impacts that may result in lower stress transfer from polymer matrix to ceramic particles with mesh- vs. finger-like pore structures. First, stress on the BT particles will have higher directional variability and will be, on average, poorly aligned with the direction of poling in the case of mesh-like pores. Second, higher localized shear stresses in mesh-like pores are more likely to result in shifting BT particle orientations during compression compared to finger-like pores. As particles rotate in different planes, piezoelectric output voltage will be reduced due to decreased net polarization of the film. It is hypothesized that these factors result in the observed difference in the piezoelectric voltage response between the two structures, with the DI film (pure finger-like morphology) having the largest voltage response despite having the highest porosity and lowest Young's modulus (Table 1). Of the two mechanisms by which pore structure affects particle stress transfer, it is likely that particle rotation effects are less significant compared to variations in localized stress states around pores. In the finite element simulations of film deformation with mesh- and finger-like pore structures, local displacement of the simulation mesh was generally small (<1 nm), making significant rotation on the scale of the 150 nm particles unlikely. Two additional morphologies of the finger-like pore structure were simulated in COMSOL Multiphysics® to explore the effect of pore dimensions on resulting stress transfer within the films (Supporting Information Table S3). The results indicate that finger-like pores should be made as thin and densely concentrated as possible to maximize piezoelectric output of porous ceramic-polymer composites.

4. Conclusion

Experimental results show a variation in piezoelectric voltage of up to 7x in BT-PVDF composite films depending on the porosity and morphology of the films. The piezoelectric response of films under compressive loading reveals greater V_{pp} with increasing porosity and increasing finger-like structures (400 mV for the finger-like DI film vs. 57 mV for the mesh-like DI45E film under 3 N compression). Finite element simulations indicate that finger-like pore structures have more ordered stress distribution compared to mesh-like structures, with a well-aligned compressive stress constituting the majority of stresses in the finger-like films. The mesh-like structure has poor alignment between stresses and large variations in stress values throughout the

structure with the presence of large shear stresses between pore connections. The resulting stress on BT particles in mesh-like structures will be less aligned than in finger-like pores, reducing piezoelectric voltage. It is also probable that finger-like pores provide more uniform stress transfer to BT particles along cavity walls, while mesh-like structures may allow particles to shift alignment during deformation. In combination, these factors likely produce the differences in piezoelectric performance observed with changing film morphology. The stress transfer mechanisms explored here are expected to apply more generally to other piezoelectric matrix-filler combinations employing flexible polymers (including PVDF-TrFE) and nanoscale ceramic filler particles (including PZT). The results indicate that the pore structure of the polymer matrix is crucial to good piezoelectric output in ceramicpolymer piezoelectric thin films and should be considered at least as important as film stiffness and overall porosity. Future work could explore orientation effects of BT particles within the films, as well as the effects of filler ratio, pore size and total pore volume on stress distribution. Pores could be controlled through other synthesis methods to further examine geometries not available through coagulation baths [38]. Rate and frequency effects, as well as bending studies, are also of interest for future study of porous piezoelectric ceramic-polymer composite films.

CRediT authorship contribution statement

Tim Kowalchik: Conceptualization, Methodology, Software, Validation, Investigation, Writing, review, editing, Analysis, Resources. Fariha Khan: Conceptualization, Methodology, Validation, Investigation, Writing, Analysis, Resources. Katrina Le: Investigation, Validation. Paige Leland: Investigation, Validation. Shad Roundy: Conceptualization, Methodology, Writing, Review, Supervision. Roseanne Warren: Conceptualization, Methodology, Writing, editing, Supervision, Funding acquisition, Project administration.

Declaration of Competing Interest

The authors declare that they have no known competing financial interests or personal relationships that could have appeared to influence the work reported in this paper.

Data Availability

Data will be made available on request.

Acknowledgments

This work is supported by the National Science Foundation (Award No. 1936636). The authors are grateful to the staff of the University of Utah Nanofab, Surface Analysis Lab, and Materials Characterization Lab for their assistance.

Supporting information

EDS measurements of BT-PVDF composite films.

FTIR measurements of BT-PVDF composite films.

FTIR measurements of PVDF phase in porous/nonporous BT-PVDF films.

Tensile stress strain curves of BT-PVDF films (Young's modulus calculation).

Compressive loading: 5 N DI film force-voltage plot.

V_{pp} response over time.

Piezoelectric coefficient comparisons.

Compliance vs. Vpp.

Alternative finger-like pore geometry simulations for stress comparisons.

Appendix A. Supporting information

Supplementary data associated with this article can be found in the online version at doi:10.1016/j.nanoen.2023.108276.

References

- [1] F. Khan, T. Kowalchik, S. Roundy, R. Warren, Stretching-induced phase transitions in barium titanate-poly(vinylidene fluoride) flexible composite piezoelectric films, Scr. Mater. 193 (2021) 64–70, https://doi.org/10.1016/j.scriptamat.2020.10.036.
- [2] S. Banerjee, S. Bairagi, S. Ali, A critical review on lead-free hybrid materials for next generation piezoelectric energy harvesting and conversion, Ceram. Int. 47 (2021) 16402–16421, https://doi.org/10.1016/j.ceramint.2021.03.054.
- [3] M. Lee, S. Cho, J. Park, Y. Jeong, Ferroelectric and piezoelectric properties of BaTiO₃-templated 0.36BiScO₃-0.64PbTiO₃ thick films for piezoelectric device applications, J. Asian Ceram. Soc. 10 (2022) 138–149, https://doi.org/10.1080/ 21870764.2021.2024964.
- [4] R. Surmenev, et al., Hybrid lead-free polymer-based nanocomposites with improved piezoelectric response for biomedical energy-harvesting applications: a review, Nano Energy 62 (2019) 475–506, https://doi.org/10.1016/j. nanoen.2019.04.090.
- [5] A. Chiolerio, et al., Effect of the fabrication method on the functional properties of BaTiO₃: PVDF nanocomposites, J. Mater. Sci. 48 (2013) 6943–6951, https://doi. org/10.1007/s10853-013-7500-9.
- [6] Y. Yang, et al., Flexible piezoelectric pressure sensor based on polydopamine-modified BaTiO₂/PVDF composite film for human motion monitoring, Sens. Actuators, A: Phys. 301 (2020), 111789, https://doi.org/10.1016/j.sna.2019.111789.
- [7] S. Ham, et al., Kinetic motion sensors based on flexible and lead-free hybrid piezoelectric composite energy harvesters with nanowires-embedded electrodes for detecting articular movements, Comp. Part B: Eng. 212 (2021), 108705, https:// doi.org/10.1016/j.compositesb.2021.108705.
- [8] Z. Xu, et al., Flexible energy harvester on a pacemaker lead using multibeam piezoelectric composite thin films, ACS Appl. Mater. Interfaces 12 (2020) 34170–34179, https://doi.org/10.1021/acsami.0c07969.
- [9] H. Zhang, et al., Ultrahigh augmentation of flexible composite-based piezoelectric energy harvesting efficiency via polymer-impregnated nanoparticles network within 3D cellulose scaffold, Comp. Part B. Eng. 236 (2022), 109813, https://doi. org/10.1016/j.compositesb.2022.109813.
- [10] Y. Ko, et al., Flexible Pb(Zr_{0.52} Ti_{0.48})O₃ films for a hybrid piezoelectric-pyroelectric nanogenerator under harsh environments, ACS Appl. Mater. Interfaces 8 (2016) 6504–6511, https://doi.org/10.1021/acsami.6b00054.
- [11] Y. Zhang, et al., Aligned porous barium titanate/hydroxyapatite composites with high piezoelectric coefficients for bone tissue engineering, Mater. Sci. Eng. C. 39 (2014) 143–149. https://doi.org/10.1016/j.msec.2014.02.022.
- [12] A. Ramadoss, et al., Piezoelectric-driven self-charging supercapacitor power cell, ACS Nano 9 (2015) 4337–4345, https://doi.org/10.1021/acsnano.5b00759.
- [13] M. Darestani, H. Coster, T. Chilcott, Piezoelectric membranes for separation processes: operating conditions and filtration performance, J. Membr. Sci. 435 (2013) 226–232, https://doi.org/10.1016/j.memsci.2013.02.024.
- [14] M. Abolhasani, et al., Hierarchically structured porous piezoelectric polymer nanofibers for energy harvesting, Adv. Sci. 7 (2020) 2000517, https://doi.org/ 10.1002/advs.202000517
- [15] K. Maeda, et al., Preparation of barium titanate porous ceramics and their sensor properties, J. Ceram. Soc. Jpn. 121 (2013) 698–701, https://doi.org/10.2109/ icersi2 121 698
- [16] S. Cha, et al., Porous PVDF as effective sonic wave driven nanogenerators, Nano Lett. 11 (2011) 5142–5147, https://doi.org/10.1021/nl202208n.
- [17] J. Roscow, J. Taylor, C. Bowen, Manufacture and characterization of porous ferroelectrics for piezoelectric energy harvesting applications, Ferroelectr 498 (2016) 40–46, https://doi.org/10.1080/00150193.2016.1169154.

- [18] J. Roscow, et al., Understanding the peculiarities of the piezoelectric effect in macro-porous BaTiO₃, Sci. Technol. Adv. Mater. 17 (2016) 769–776, https://doi. org/10.1080/14686996.2016.1245578.
- [19] S. Karmakar, R. Kiran, C. Singh, R. Vaish, Effect of Porosity on Energy Harvesting Performance of 0.5Ba(Ca_{0.8}Zr_{0.2})O₃-0.5(Ba_{0.7}Ca_{0.3})TiO₃ Ceramics: A Numerical Study, Energy Technol. 8 (2020) 1901302, https://doi.org/10.1002/ epts 201001302
- [20] T. Zeng, X. Dong, S. Chen, H. Yang, Processing and piezoelectric properties of porous PZT ceramics, Ceram. Int. 33 (2007) 395–399, https://doi.org/10.1016/j. ceramint.2005.09.022.
- [21] P. Lee, et al., Development of porous ZnO thin films for enhancing piezoelectric nanogenerators and force sensors, Nano Energy 82 (2021), 105702, https://doi. org/10.1016/j.nanoen.2020.105702.
- [22] R. Guo, C. Wang, A. Yang, Effects of pore size and orientation on dielectric and piezoelectric properties of 1-3 type porous PZT ceramics, J. Eur. Ceram. Soc. 31 (2011) 605–609, https://doi.org/10.1016/j.jeurceramsoc.2010.10.019.
- [23] S. Xie, et al., Flexural fracture mechanisms and fatigue behaviors of Bi4Ti3O12-based high-temperature piezoceramics sintered at different temperatures, Ceram. Int. 44 (2018) 16758–16765, https://doi.org/10.1016/j.ceramint.2018.06.107.
- [24] T. Zeng, et al., The dielectric breakdown properties of porous PZT95/5 ferroelectric ceramics, Ferroelectr 478 (2015) 118–126, https://doi.org/10.1080/ 00150193.2015.1011528.
- [25] T. Le, et al., Piezoelectric nanofiber membrane for reusable, stable, and highly functional face mask filter with long-term biodegradability, Adv. Funct. Mat. 32 (20) (2022), https://doi.org/10.1002/adfm.202113040.
- [26] H. Mao, et al., Self-cleaning piezoelectric membrane for oil-in-water separation, ACS Appl. Mat. Interfaces 10 (21) (2018), https://doi.org/10.1021/ accami.8h03051
- [27] W. Qian, et al., Piezoelectric materials for controlling electro-chemical processes, Nano Micro Lett. 12 (2020), https://doi.org/10.1007/s40820-020-00489-z.
- [28] T. Franke, et al., Surface acoustic wave actuated cell sorting (SAWACS, Lab Chip 6 (2010), https://doi.org/10.1039/b915522h.
- [29] Mulder, M. Membrane preparation. In Encyclopedia of Separation Science: Phase inversion membranes, Academic Press, 2000, pp. 3331–3346. https://doi.org/ 10.1016/B0-12-226770-2/05271-6.
- [30] J. Cao, H. Zhang, W. Xu, X. Li, Poly(vinylidene fluoride) porous membranes precipitated in water/ethanol dual-coagulation bath: the relationship between morphology and performance in vanadium flow battery, J. Power Sources 249 (2014) 84–91, https://doi.org/10.1016/j.jpowsour.2013.10.069.
- [31] M. Thürmer, et al., Effect of non-solvents used in the coagulation bath on morphology of PVDF membranes, Mater. Res. 15 (2012) 884–890, https://doi.org/ 10.1590/S1516-14392012005000115.
- [32] A. Ahmad, W. Ramli, W. Fernando, W. Daud, Effect of ethanol concentration in water coagulation bath on pore geometry of PVDF membrane for Membrane Gas Absorption application in CO₂ removal, Sep. Purif. Technol. 88 (2012) 11–18, https://doi.org/10.1016/j.seppur.2011.11.035.
- [33] S.P. Deshmukh, K. Li, Effect of ethanol composition in water coagulation bath on morphology of PVDF hollow fiber membranes, J. Membr. Sci. 150 (1998) 75–85, https://doi.org/10.1016/S0376-7388(98)00196-3.
- [34] J.M. Kenney, S. Roth, Room temperature poling of Poly(Vinylidene fluoride) with deposited metal electrodes, J. Res. Natl. Bur. Stand. 84 (1979) 447–453, https://doi.org/10.6028/JRES.084.022.
- [35] S. Qin, X. Zhang, Z. Yu, F. Zhao, Polarization study of poly(vinylidene fluoride) films under cyclic electric fields, Polym. Eng. Sci. 60 (2020) 645–656, https://doi. org/10.1002/pen.25323.
- [36] S. Shin, et al., Hemispherically aggregated BaTiO₃ nanoparticle composite thin film for high-performance flexible piezoelectric nanogenerator, ACS Nano 8 (2014) 2766–2773, https://doi.org/10.1021/nn406481k.
- [37] Olszowy, M. Piezoelectricity and dielectric properties of PVDF/BaTiO3 composites. Proc. SPIE 3181, Dielectr. Relat. Phenom.: Mater. Phys.-Chem. Spectr. Investig. Appl. (1997). https://doi.org/10.1117/12.276252.
- [38] Y. Zhang, H. Sun, C.K. Jeong, Biomimetic Porifera skeletal structure of lead-free piezocomposite energy harvesters, ACS Appl. Mater. Interfaces 10 (2018) 35539–35546, https://doi.org/10.1021/acsami.8b13261.